Revisiting the Basel-1 Hydraulic Stimulation with a 3D Coupled Hydro-Mechanical Model

Regina Fakhretdinova[1], Alexis Sáez[2], Brice Lecampion[1] and Andrés Alcolea[3]

[1]Geo-Energy Laboratory, EPFL, Lausanne, 1015, Switzerland

[2] Caltech, Division of Geological and Planetary Sciences, Pasadena, California, 91125

[3]Geo-Energie Suisse AG, Reitergasse 11, Zürich, 8004, Switzerland

regina.fakhretdinova@epfl.ch

Keywords: hydraulic stimulation, Basel, numerical modeling, hydro-mechanical coupling

ABSTRACT

On the 2nd of December 2006, the Basel-1 well was hydraulically stimulated with the aim of significantly increasing reservoir transmissivity and achieving economical geothermal energy fluxes. Over six days, 11,500 cubic meters of water were injected into a 371-meter-long openhole section of the well, reaching a depth of 5 kilometers. As seismic activity began to rise, peaking at up to 200 events per hour, the injection rate was reduced, and eventually, the well was temporarily shut down for five hours. Despite these measures, an earthquake of ML 3.4 occurred (and was felt in the city of Basel) just before the wellhead pressure was fully released. In light of this significant seismic event, the project was ultimately abandoned. Over the years, the Basel hydraulic stimulation and its associated seismicity have been extensively studied. Experts have examined various aspects, including stress levels and hydraulic and microseismic data. Although numerous numerical models have been developed, none have yet succeeded in accurately and comprehensively reproducing both the measured pressure and the spatiotemporal microseismicity migration.

In this paper, we revisit the 2006 Basel-1 well stimulation using a fully coupled hydro-mechanical model to reproduce both pressure data and the spatio-temporal microseismicity distribution. In our model, microseismicity is assumed to be triggered by both the increase in pore pressure and the transfer of stress due to aseismic slip. Thus, the microseismicity cloud provides an indirect measure of the evolution of aseismic slip when this mechanism is dominant. Our primary model simulates the first activated group of events, which represents the largest stimulated structure, as a single slipping patch that propagates aseismically in pure shear mode. Key parameters, such as maximum horizontal stress, friction, dilatancy, and joint closure nonlinearity are varied to align with observed pressure and microseismic migration. We find that early pressure drops can be explained by a simple linear relation between dilatancy and slip, whereas the later pressure response requires incorporating the nonlinear effects of joint closure.

Our results show that a coupled hydro-mechanical model, initially restricted to a single plane with linear slip-weakening friction and nonlinearly varying dilatancy and permeability, successfully reproduces the evolution of the well pressure data and the migration of the observed micro-seismicity of the first group.

1. INTRODUCTION

The Deep Heat Mining Project in Basel aimed to create a high-conductive fracture network to mine heat and produce electricity. The first preparations for the project began in February 2006 when the microseismic monitoring array was put into operation. Following that, between May and October, the well Basel-1 was drilled up to 5 km TVD through 2.5 kilometers of sedimentary rocks and 2.5 kilometers of the granitic basement. The last 371 meters of the well were left uncased and uncemented – providing an openhole section for fluid injection. The next steps included extensive logging and testing phases. Finally, the granite in the openhole section was hydraulically stimulated to enhance reservoir permeability. However, during the hydraulic stimulation, the injection had to be stopped after 6 days due to a rise in the microseismic activity with events up to 2.6 in local magnitude. A large seismic event of magnitude of 3.4 ML occurred five hours after shut-in in the proximity to the well, and three aftershocks followed in the next 56 days. The project was subsequently abandoned as a result. Over the years, the Basel hydraulic stimulation and induced events have received a lot of attention from various researchers – analyzing stress, hydraulic, and microseismic data.

Numerous models have been developed to investigate hydraulic stimulation processes and the induced seismicity observed in Basel. Early studies focused on fluid flow dynamics during hydraulic stimulation, emphasizing the complex interplay between pore pressure changes and seismic activity (Terakawa, et al., 2012; Terakawa, 2014; Mukuhira, et al., 2017). Some models incorporated poroelastic effects (Miller, 2012; Boyet, et al., 2022; Boyet , et al., 2023; Boyet, et al., 2023) while omitting fault deformation. As research advanced, efforts were made to better understand the mechanisms behind pore pressure migration and its relationship with seismicity, particularly during fluid injection and subsequent shut-in phases (Miller, 2012; Mukuhira, et al., 2017). These studies highlighted the significance of factors such as stress state, fluid viscosity, and flow nonlinearity in influencing fracture behavior and seismic responses. Recent three-dimensional models (Lei, et al., 2016; Sandro, et al., 2019; Lei, et al., 2022) have further refined the understanding of these interactions by incorporating constitutive equations to describe mechanical behavior and employing hydromechanical coupling to capture the intricate relationships between fluid flow and rock deformation.

Despite all efforts, no physics-based model has been capable of accurately reproducing both the measured pressure response and the observed migration of the recorded microseismic events.

In this work, we use a coupled hydro-mechanical model to reproduce both the injection and the microseismicity migration. We assume that the microseismic activity tracks the propagation of an otherwise aseismic macroscopic frictional rupture. The latter allows us to model the microseismicity propagation as a single axisymmetric slipping patch propagating in pure shear mode along a planar interface. We perform 3D axisymmetric hydromechanical simulations of the Basel hydraulic stimulation using the exact injection schedule. We use a new numerical solver (Lecampion, et al., to appear in 2025) to solve hydromechanical problems accounting for non-linear flow in frictional weakening shear-reactivated discontinuities in a fully coupled implicit manner.

2. CURRENT STATE OF KNOWLEDGE

This section presents an overview of the available geological, geomechanical, and hydraulic data for the Basel deep geothermal site. The aim is to synthesize the critical information derived from various datasets and the published literature, including televiewer logs, borehole measurements, and pre-stimulation tests, to provide a comprehensive understanding of the site's subsurface conditions.

2.1 Location

The Basel deep geothermal site is located within the city of Basel, in the southeastern area that forms part of the Rhine Rift Valley (or Upper Rhine Graben). The Upper Rhine Graben is a significant rift that extends from Basel in the south to the cities of Frankfurt and Wiesbaden in the north (Figure 1). It is approximately 350 kilometers long and averages 50 kilometers in width.

The southern part of the rift, where it intersects the Jura Mountains, is the most seismically active zone in the Upper Rhine Graben. Historically, the most catastrophic seismic event occurred near Basel in 1356, registering a magnitude between 6.5 and 6.9 (Giardini, et al., 2004). Nowadays, general seismic activity on the rift is relatively moderate (Ustazewski & Schmid, 2007) and is characterized by the reactivation of basement fracture zones striking NNE, ENE, and NW.

2.2 Geological and Geomechanical Description

Between May and October 2006, the well Basel-1 was drilled vertically up to 5 km TVD through about 2.5 km of sedimentary rocks and 2.5 km of the granitic basement (Figure 1). Sedimentary rocks are mainly composed of pre-rift, syn-rift, and post-rift sediments. The transition to a crystalline basement occurs through Permian sandstones and conglomerates (764 m thick) (Baisch & Vörös, 2009).

The crystalline basement is composed exclusively of undeformed plutonic rocks with no metamorphic-type inclusions, indicating that the rock mass is relatively homogeneous and consistent in its mineralogical composition. The rock type is mostly granitoid rocks with less than 1% aplite and lamprophyre (Kaeser B., 2007). The granitoid rock composition in Basel includes 45% I-type granite, 45% I-type monzogranite, and 10% monzonite. The dominant mineral composition of the crystalline basement in Basel contains common minerals in granitoid rocks like plagioclase, K-Feldspar, and quartz, which contribute to hardness and resistance to weathering; hornblende and biotite, which contribute to the increase of the rock's density and mechanical strength; and titanite. Further, down the borehole, the rocks contain higher concentrations of hornblende and biotite and have a reduced quartz content, making the formation denser and stronger with increasing depth but more prone to chemical weathering than quartz-rich rocks.

The openhole section of the borehole, spanning from 4629 meters to 5000 meters deep, covers a length of 371 meters with a diameter of 22 centimeters and is completely embedded within the crystalline basement. This basement section was scanned with an acoustic borehole imager to identify both natural and induced fractures, including tensile fractures and borehole breakouts. The fracture density below 3.0 km (including the openhole section) varies from 0.2 to 0.3 fractures/m (Ziegler, et al., 2015) and contains two major fractured zones at 4700 and 4835 meters depth (Ladner, et al., 2008).
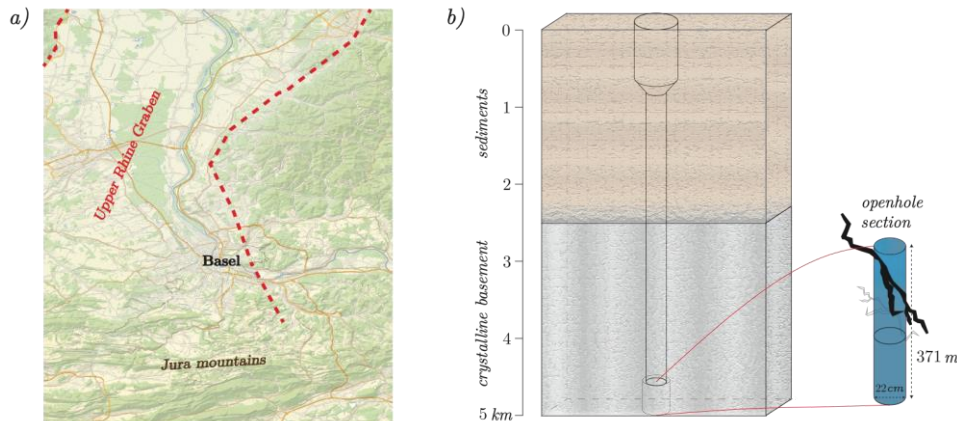

Figure 1: *a)* Schematic map of the southern Upper Rhine Graben. *b)* Representation of the Basel-1 well depicting the 371-meter openhole section. The well extends to a depth of 5 kilometers, penetrating sedimentary layers and granite. The deviation from

vertical is less than 8° overall and reduces to 4° above 3.6 km. The largest identified fracture structure intersects the borehole at 4.7 km, as the televiewer log shows. The highlighted fracture illustrates the main activated structure during hydraulic stimulation.

2.3 Stress Field

The stress field in the Basel-1 site was not determined using any hydrofracturing tests. It was mostly inferred from borehole breakout, drilling-induced tensile fracture analysis, and density log data. These analyses provide key constraints on the stress regime, including its orientation and magnitudes at various depths.

2.3.1 Orientation

Numerous studies have employed fault plane solutions of earthquakes from naturally occurring seismic events in the crystalline basement of the Upper Rhine Graben to deduce the stress field characteristics in this region (Plenefisch & Bonjer, 1997; Deichmann, et al., 2000; Kastrup, et al., 2004). These investigations consistently demonstrate that near Basel, situated in the Northern Alpine foreland, one of the principal stress directions is oriented vertically, while the remaining two principal directions are horizontal. The optimal stress tensor configuration derived from these data suggests a transition from pure strike-slip to normal faulting mechanisms with increasing depth, although occasional local stress inhomogeneities, such as those producing thrust faulting, may occur. Fault plane solutions obtained from the Basel-1 site primarily demonstrate strike-slip faulting along north-south trending fault planes, with a smaller portion of the solutions indicating normal faulting. This aligns well with the strike-slip-dominated stress regime of the Upper Rhine Graben.

Analyses of borehole breakout measurements and drilling-induced tensile fractures have further refined the understanding of the stress tensor orientation in the Basel-1 well (Valley, et al., 2009; Dahrabou, et al., 2022). These studies estimate S_{hmin} azimuth to be $54 \pm 14°$ and S_{Hmax} to strike $144 \pm 14°$, representing an average for the openhole section. A similar analysis was conducted for the well OTER 2, located only 1 km southeast of the Basel-1 well. The results for the OTER 2 (S_{Hmax} strike is $140 \pm 16°$) are well aligned with the values obtained for Basel-1.

2.3.2 Magnitudes

Vertical principal stress S_V magnitude

The magnitude of vertical stress can be derived from density logs obtained from the sedimentary section of well OTER 2 and the crystalline basement of well Basel-1. Integrating this data gives

$$S_V = 24.9z[km], [MPa] \tag{1}$$

with z in kilometers. It was pointed out (Valley & Evans, 2009), that this stress gradient overestimates vertical stress at the top of the openhole by 0.6 MPa and underestimates it by 3 MPa at the bottom. Correcting the mean density of the rock overlying the openhole section, the authors obtained

$$S_V = 26.3z - 4, [MPa] \tag{2}$$

that is used in this work.

Horizontal principal stress S_{hmin} and S_{Hmax} magnitudes

Some general bounds can be easily obtained from the following observations: since no pressure-limiting behavior was observed — indicating that fractures did not open — it can be inferred that the minimum effective stress is greater than the maximum stimulation overpressure. The first attempt to identify minimum S_{hmin} and maximum S_{Hmax} principal stress magnitudes was performed using RACOS (Rock Anisotropy Characterization on Samples, (Braun, 2007) measuring P and S wave velocities on the core sample from 4911 m depth. Unfortunately, no description of the experiment is available. The horizontal principal stress components obtained in the experiment (Häring, et al., 2008) are $S_{hmin} = 84$ MPa and $S_{Hmax} = 122$ MPa. Using this data, Häring then applied a linear model fit, assuming zero traction at the surface, to calculate:

$$S_{hmin} = 17.1 \, z[km], [MPa] \tag{3}$$

$$S_{Hmax} = 32.6 \, z[km], [MPa] \tag{4}$$

This model was later argued by Valley and Evans in 2019 as being unrealistic. They argued that the diminishing breakout widths with increased depth, as observed in their analysis, indicate that the stress gradient must be relatively small. Their proposed correction is

$$S_{hmin} = 7z[km] + 42, [MPa] \tag{5}$$

$$S_{Hmax} = 5z[km] + 90, [MPa] \tag{6}$$

The accuracy of this model greatly depends on the failure criterion applied to determine borehole failure, which significantly influences the estimates of S_{Hmax} magnitude. For this reason, another model was proposed (Dahrabou, et al., 2022) to correct the S_{Hmax} estimate

$$S_{Hmax} = 5z[km] + 170, [MPa] \qquad (7)$$

where the authors performed sensitivity analysis on the choice of a failure criterion.

Despite extensive efforts to define the maximum horizontal stress, the results from Valley & Evans (2019) and Dahrabou et al. (2022) cannot be directly applied to our analysis. When projecting these stress tensors onto the largest activated fault plane in Basel and calculating the Coulomb distance to failure with a friction coefficient f_p of 0.66, the outcomes yield values of 11.4 MPa and -3.3 MPa, respectively. The former value, which will be explained further in the Discussion section, is excessively high, while the latter suggests pre-injection failure of the fault. Consequently, we have adjusted the S_{Hmax} values to reflect a more realistic range between the findings of these two studies.

2.4 Young's Modulus and Poisson's Ratio

The elastic properties were determined from a multistage confined compression test conducted on a single core sample of Basel monzogranite. The core, measuring 34 mm in diameter and 70 mm in length, was extracted from the Basel-1 borehole at depths ranging from 4896.5 m to 4906.5 m. The test yielded a Young's modulus of 39 GPa and a Poisson's ratio of 0.22 (Braun, 2007). In contrast, sonic and density logs taken from depths of 4896.5 m to 4906.5 m reveal an average dynamic Young's modulus of 80 GPa, which correlates to a static modulus of approximately 60 GPa using a logarithmic relation (Eissa & Kazi, 1988). The lower values observed in the core compression test are attributed to damage incurred during the retrieval of the sample (Valley & Evans, 2009). Based on these measurements, we conclude that the values below 60 GPa are more reasonable due to the intrinsic presence of discontinuities at larger scales in rock masses, resulting in a decrease in macroscopic properties (Kachanov., 1991). Therefore, we allow Young's modulus to vary within a range between 20 GPa and 60 GPa on a metric scale.

2.5 Pre-stimulation Test Analysis

A well test was performed before the high-pressure hydraulic stimulation. The goal of this pre-stimulation well test in Basel-1 was to define flow regimes and subsequently determine the initial hydraulic properties of its openhole section (Figure 2). All measurements for the pre-stimulation test sequence were made at the wellhead. The well was first repeatedly opened and shut to remove the mud in the wellbore and to obtain the undisturbed formation pressure. The pressure did not fully stabilize during these periods (negative times in Figure 2) and continued to increase with an approximate slope of 3.36 Pa/s. We remove this trend from the pressure record of the pre-stimulation test to account for formation pressure and analyze a sequence of three injection rate steps followed by a shut-in period (positive times in Figure 2).
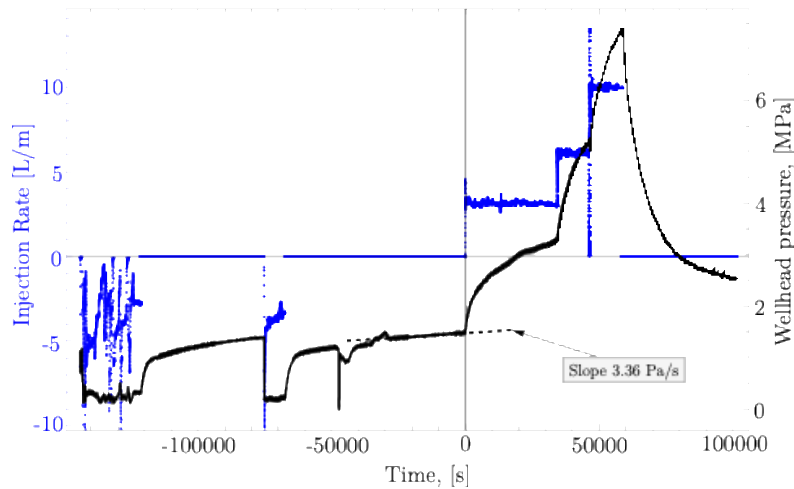

Figure 2: Pre-stimulation test sequence.

Pressure-derivative analysis

Figure 3 shows the pressure-derivative analysis for the first two injection steps of the pre-stimulation test sequence. This analysis primarily aims to identify the flow regimes (Bourdet, et al., 1989), with a particular emphasis on determining whether radial flow was established during the test. Taking a derivative from the lowpass filtered (cutoff frequency 0.001) overpressure record with respect to the logarithm of time helps to identify all the regimes when overpressure Δp follows a time function $C * t^{\kappa}$, where C and κ are constants. Indeed, the derivative $d\Delta p/dLn(\Delta t)$ is $\kappa * \Delta p$; therefore, the derivative plotted alongside the original record on the Log-Log scale represents a constant κ shift along the y-axis. This logarithmic derivative is particularly useful in pinpointing radial flow, as it reveals stabilization in overpressure at late times.

From the first step of the pre-stimulation injection sequence, one can identify three regimes: for times $t < 200$ s the flow is dominated by wellbore storage; for $200 < t < 2000$ seconds, the overpressure aligns with its derivative shifted by $\kappa \approx 0.66$ on the y-axis (Log-Log

scale), suggesting flow through multiple fractures; for $t > 2000$ seconds, the pattern shifts from bilinear to a transition towards radial flow. However, the overpressure does not stabilize, and the derivative shows abrupt fluctuations, making it difficult to assess definitively.

In the later stages, specifically during the second and third steps of the pre-stimulation injection sequence, the filtered pressure derivative stabilizes significantly. By the end of the second step, the evidence suggests an approaching stabilization, likely indicative of dominant radial flow.
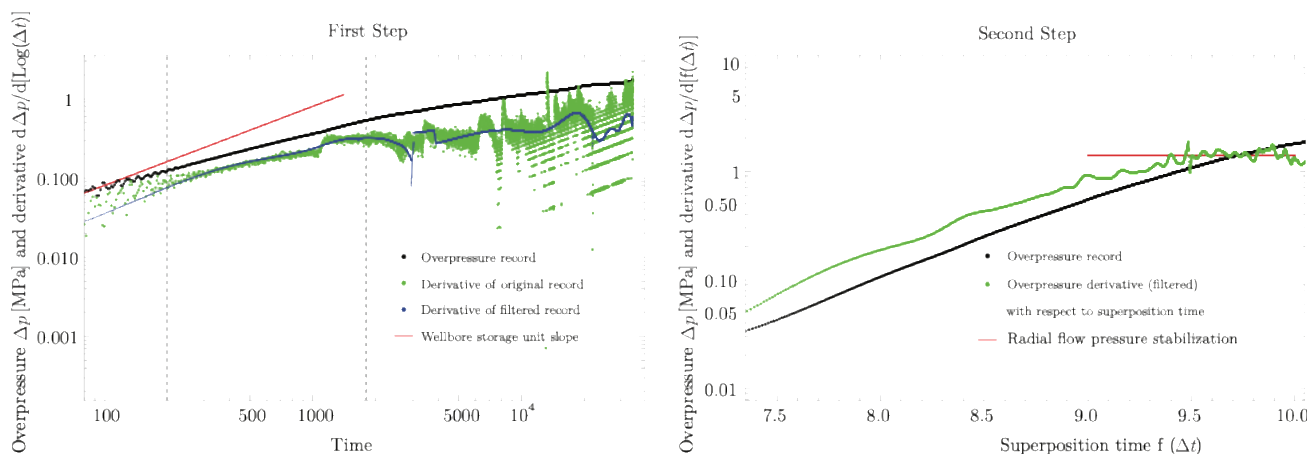

Figure 3. Panel (a): First injection step of pre-stimulation test sequence. Panel (b): Second injection step of pre-stimulation test sequence.

Determination of the initial hydraulic properties

In many reservoirs, assuming a radial flow regime becomes increasingly valid as transient early-time effects diminish and before the flow reaches reservoir boundaries. We performed a preliminary fit of the pre-stimulation test with the analytical solution for the radial flow of a slightly compressible fluid from a point source in a homogeneous isotropic reservoir accounting for wellbore storage (Van Everdingen & Hurst, 1949) to define an initial range for transmissibility $k * h$ and wellbore storage C_s. The results of the fit are presented in **Error! Reference source not found.** and Figure 4.
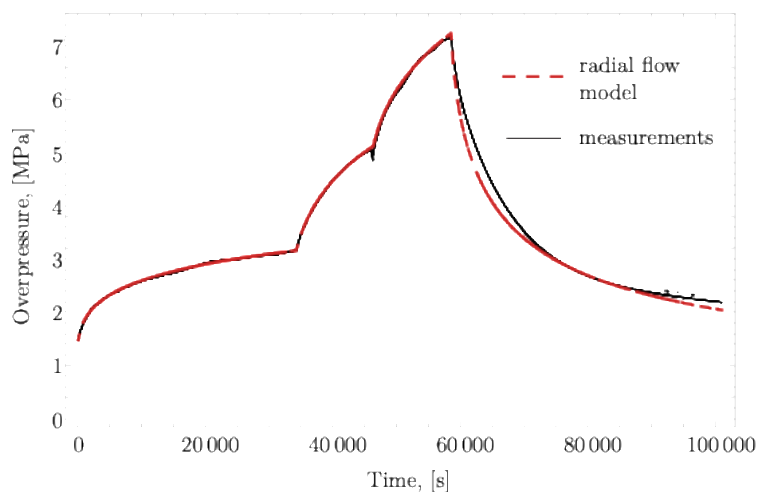

Figure 4: Overpressure measurements during three injection rate steps in black and shut-in fitted by an analytical model assuming radial flow and accounting for wellbore storage (Van Everdingen & Hurst, 1949).

Table 1. Best fit parameters obtained for each step

Step	Transmissibility $k * h$, [m^3]	Wellbore storage C_s, [m^{3}Pa^{-1}]
Step 1	$1.95 * 10^{-15}$	$6.5 * 10^{-8}$
Step 2	$1.43 * 10^{-15}$	$9.48 * 10^{-8}$

Step 3	$2.34 * 10^{-15}$	$5.92 * 10^{-7}$
Shut-in	$1.22 * 10^{-15}$	$4.36 * 10^{-7}$

2.6 Seismic Catalogue

The seismic monitoring network included six borehole seismometers installed at depths from 320 m to 2,745 m near the injection well and 30 surface stations spread across the Basel area. The Swiss Seismological Service (SED) operated the surface network, while Geothermal Explorers (GEL), the operator of the EGS project, installed and managed the borehole network (Dyer, et al., 2008; Dyer, et al., 2010).

During hydraulic stimulation, 13,500 events were detected, and 2,400 of those were located in real-time with an absolute accuracy of approximately 100 meters for the hypocenter location. Further analysis enhanced the resolution of the microseismic event locations to 25 meters by identifying events with similar waveforms and then using cross-correlation to refine S-wave travel time picks. The identified clusters were associated with the focal mechanisms of large events published by SED. The overall microseismic cloud forms a steeply dipping structure that is well-aligned with the direction of maximum horizontal stress S_{Hmax}. This study employs the seismic catalog of Dyer, et al., 2010 provided by Geo-Energy Suisse (Alcolea, et al., 2011), building on previous research (Häring, et al., 2008; Dyer, 2008). The catalog contains 3,511 located seismic events with local magnitudes ranging $-1 \leq M_L \leq 3.4$. Of these, 2,860 (approximately 81%) were clustered solely based on waveform correlation without considering spatial geometry. These clusters are referred to as the Semore clusters in the report (Alcolea, et al., 2011) and in the following.
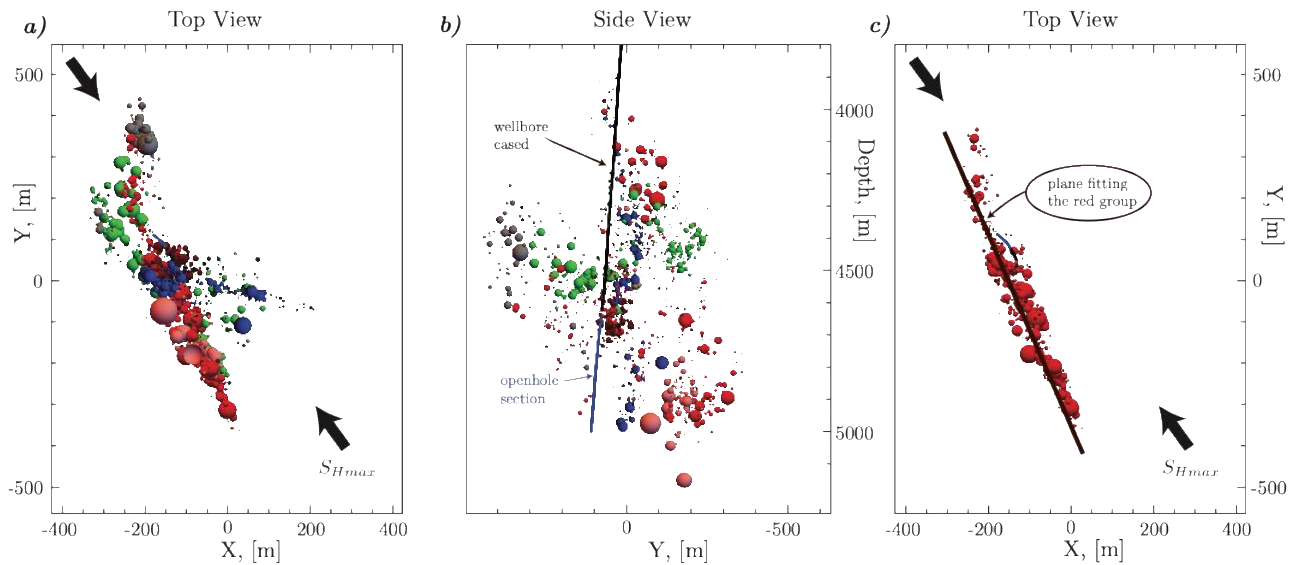

Figure 5: Top and side views of 81% of all located seismic events. Each color represents a group of events with similar waveforms and orientations. Six groups of events were identified, labeled red, maroon, blue, green, pink, and gray. The red group, which is the largest structure, intersects the borehole at a depth of 4.7 km true vertical depth. In panel (a), the top view displays the spatial distribution of the events, with the direction of maximum horizontal stress (S_{Hmax}) indicated by the arrows. Panel (b) presents the side view of the same events, with the events aligned along a steeply dipping structure. In panel (c), the top view illustrates the vertical plane fitted to the red group of cluster planes, emphasizing its steep orientation.

Since parallel faults can produce events with similar waveforms, the events within each Semore cluster may originate from different fault patches. Consequently, each cluster was fitted with multiple planes – typically two or three – resulting in a total of 42 planes. To validate the representation of these fault surfaces, the focal mechanisms of 200 events obtained by SED were compared with those derived from the cluster planes. Finally, the cluster planes were grouped into six sets based on similarly oriented planes, each represented by a distinct color (see Figure 5). This analysis enabled the geometric characterization of the stimulated reservoir (Alcolea, et al., 2011). As the last step, (Alcolea, et al., 2011) fitted one plane for each group of cluster planes and projected the hypocenters of the events onto its representative plane to calculate the stimulated area.

In this study, we focus our initial investigation on the "red group" of seismic events. This choice is based on several factors: first, the red group intersects the borehole at a depth where a significant fault zone was identified through the televiewer log; second, it was the first structure activated during the injection period and remained active for the longest time, indicating its crucial role in the dynamics of the reservoir. Notably, this group constitutes 43% of all clustered seismic events and represents the largest area of vertically dipping cluster planes. In our analysis, we compare the area affected by this group, derived from projecting the hypocenters of the red group onto its representative plane (Alcolea, et al., 2011), with our numerical simulation results. This approach relies on the assumption that microseismicity propagation results from both aseismic slip stress transfer and increases in pore pressure.

Table 2: Different groups of events and their activation times.

Group	Activation time (from the beginning of injection), [seconds]	Percentage of all clustered events, %
Red	79517	43
Maroon	87941	10
Blue	138952	13
Green	218238	22
Pink	320577	10
Gray	338079	2

3. OVERVIEW OF SEMI-ANALYTICAL MODELS

Important advances in understanding the propagation of fluid-induced frictional rupture along pre-existing fractures were made in contributions (Garagash & Germanovich, 2012; Viesca, 2021; Sáez, 2023; Sáez & Lecampion, 2023; Sáez & Lecampion, 2024). These studies have greatly enhanced our knowledge of propagation regimes and have provided insights into real-world observations. In this section, we offer a simplified overview of these contributions, which will later be applied to our analysis of the Basel dataset.

The first findings were made in the 2D plane-strain case. (Garagash & Germanovich, 2012) The authors investigated conditions leading to dynamic slip initiation in 2D under the assumptions of quasi-static linear elasticity, linear slip-weakening of friction, and pore pressure diffusion from a line source into the fault plane. They have shown that when initial shear stress (τ_o) is lower than the residual shear strength at ambient conditions (τ_r), then even if the fault transits to a dynamic propagation regime, the instability will be arrested by the limits of the pressurized zone. On the other hand, when the ambient residual shear strength is higher than the initial shear stress ($\tau_r > \tau_o$), then a dynamic rupture will always be nucleated and will not stop in the absence of any stress & material properties variation.

Viesca (2021) has provided a complete analytical solution for the case of a uniform initial state of stress, constant friction, constant hydraulic properties, and an injection performed at constant overpressure under plane-strain conditions. It was shown that the problem is governed by one dimensionless parameter, the fault injection stress parameter, which determines two limiting regimes, the so-called "marginally pressurized" and "critically stressed" regimes. Each regime corresponds to different physical mechanisms governing the fault propagation (first introduced in (Garagash & Germanovich, 2012)). The marginally pressurized limit corresponds to the case when the fluid pressure is "just sufficient" to activate the fault by reducing the shear strength. Crack propagating in this regime will always lag the fluid front. The critically stressed limit corresponds to the case when the fault is initially close to failure. For this limit, the crack front will always outpace fluid diffusion.

Sáez et al. (2021) have extended the same problem to three dimensions. The study offers a comprehensive understanding of quasi-static propagation of fault slip, assuming uniform in-situ stresses, constant friction, and constant fault permeability in 3D. It appears that in the case of a constant injection rate, the crack growth is self-similar and governed by a similar dimensionless parameter as the constant injection overpressure case in 2D. Furthermore, it was shown that in both critically stressed and marginally pressurized cases, the rupture shape is quasi-elliptical, with aspect ratios depending on Poisson's ratio and the fault injection stress parameter.

Finally, we focus on the study (Sáez & Lecampion, 2023), which plays a central role in this section. This work investigates the propagation of aseismic slip after injection is stopped ("shut-in"), using the same assumptions made in previous studies (Sáez, 2023). The study identifies key conditions under which rupture propagation occurs as discrete pulses and highlights factors that determine when the rupture stops. Importantly, it reveals that critically stressed faults – those already close to failure – can sustain rupture pulses that propagate far beyond the injection period. This can significantly expand the size of initial ruptures. The findings suggest that post-injection aseismic slip, which gradually stresses larger areas of the surrounding rock, may play a crucial role in triggering seismic events after fluid injections. This hypothesis is backed by quantitative correlations with field data that document seismicity occurring after the injection phase ends.

The relevance of this phenomenon is evident in the case of Basel, where seismic activity continued to spread after shut-in. Notably, the largest seismic event (ML 3.4) occurred five hours after shutting down the well. This delayed response strongly aligns with the critically stressed limit described by (Sáez & Lecampion, 2023), where the fault's initial proximity to failure allows for ongoing rupture propagation after shut-in. In this scenario, the rupture front outpaces the diffusion front, and the pressure profile $p(r, t_o)$ can be effectively modeled as a point force, with the pressure intensity (pressure multiplied by the area occupied by the fluid) serving as a defining characteristic of the system's behavior:

$$p(r, t_o) * Area = 2\pi \int_0^{R_{diff}(t_o)} rp(r, t_o)\, \mathrm{d}r \tag{8}$$

7

where $R_{diff}(t_o)$ is the diffusion front radius at a fixed time t_o. Now, utilizing the mass balance, the pressure intensity can be re-written in terms of injected volume V_{inj}, storage coefficient S_e, and flow zone thickness w as

$$p(r, t_o) * Area = \frac{V_{inj}(t_o)}{S_e w} \tag{9}$$

Another key assumption that can be utilized at late times is process zone localization. As the rupture expands, friction decreases only in a small region near the rupture front, while in the remainder of the rupture, it stays constant and equals its residual value. Under these circumstances, the energy balance can be expressed in a front-localized form (see (Sáez, et al., 2023) for detailed derivations). By adopting a point force approximation for pressure and constant permeability, the energy balance equation can be solved for the rupture radius:

$$R(t) = \frac{2}{\sqrt{2\pi}} \sqrt{\frac{V_{inj}(t)f_r}{S_e w(f_r \sigma_o' - \tau_o)}} \tag{10}$$

where $R(t)$ is the rupture radius, f_r the residual friction coefficient, σ_o' and τ_o are the effective initial normal and shear stress, respectively.
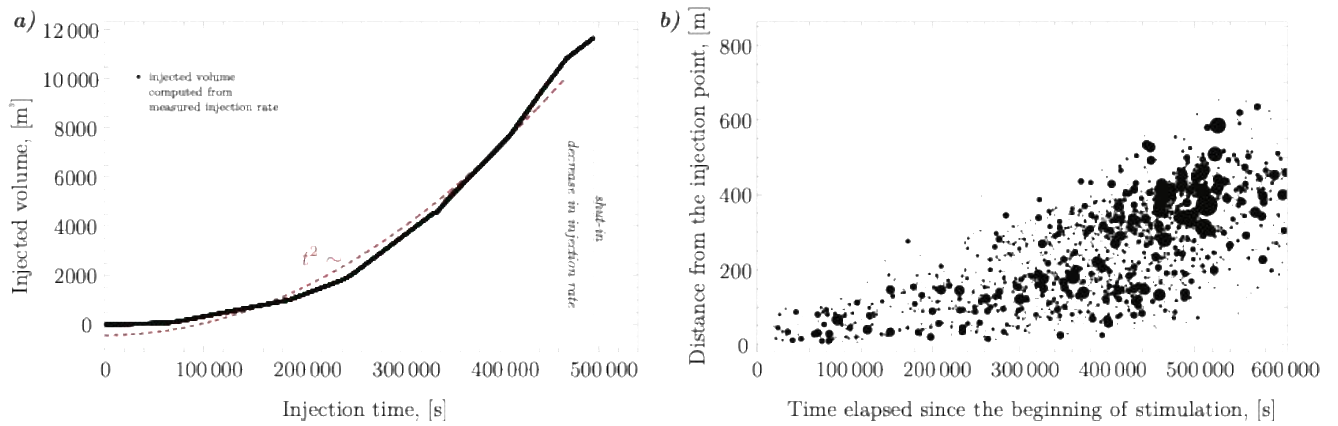

Figure 6: In panel (a), the temporal evolution of the injected volume during stimulation is approximated by a quadratic function. In panel (b), microseismicity recorded during and after the Basel stimulation test. The linear trend of the rupture front, as predicted by the semi-analytical model, agrees with observed microseismicity.

The injected volume in Basel, when plotted against time, can be closely approximated by a quadratic function, as shown in Figure 6a. In turn, equation (10) suggests that the rupture front should evolve linearly at late times, a pattern that is clearly observed in the recorded seismicity (Figure 6b). We utilize the semi-analytical solution to fit the seismic radius of the red group of events. The seismic radius is computed as follows: first, the hypocenters of the events are projected onto the best-fitting plane (see (Alcolea, et al., 2011) for further information); second, the convex and concave hulls of the projections are calculated. Thus, convex and concave hulls are polygons whose areas can be computed. From these areas, we can determine the radius of a circle that would cover the same area (simply $S = \pi R^2$) to compare the measurements with the semi-analytical solution. The main reason for doing this is that in an axisymmetric model, the Poisson's ratio is zero to ensure a circular rupture shape. Non-zero Poisson's ratios have the main effect on the aspect ratios of mixed-mode shear ruptures while keeping the shear rupture area the same (Sáez, 2023). Therefore, this assumption does not limit our investigation, as it is only crucial in relation to the rupture's geometry while keeping the total area unchanged. In this sense, we compare the areas of the clouds rather than their detailed geometric shapes.

Figure 7 presents the results of the fit, demonstrating that the semi-analytical solution provides a robust approximation of how the seismic radius evolves over time. However, the corresponding flow solution for the pressure fails to reproduce the well pressure record because it does not account for local permeability variations associated with mechanical deformation. This result is expected, as while fitting the radius, we fixed the pressure intensity computed as an integrated response over the whole area occupied by the fluid. However, the pressure measurement is local and cannot be accurately reproduced without considering permeability variations. As a result, precise local pressure analysis requires accounting for permeability variations, highlighting the limitations of using an uncoupled analytical approach.
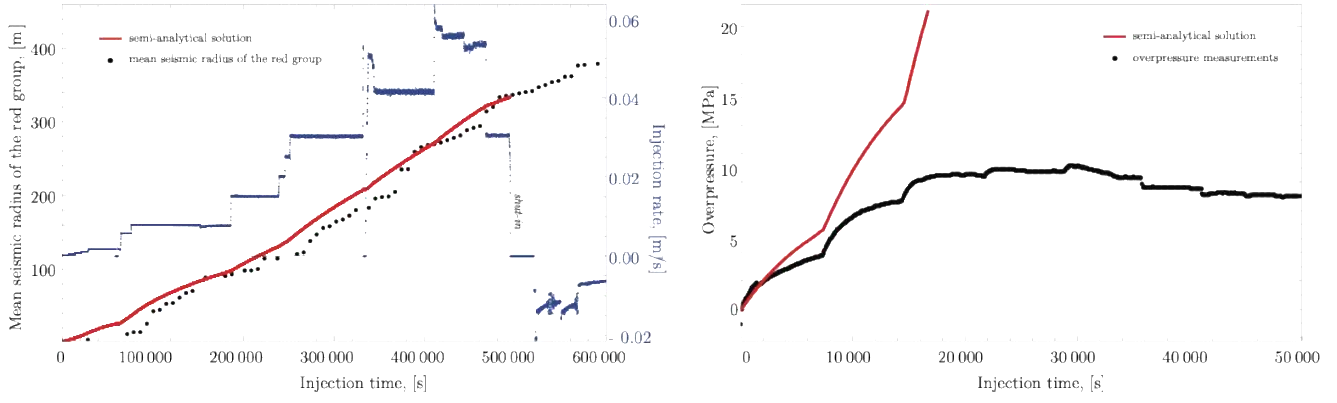
Figure 7. Panel (a): This graph shows the time evolution of seismic radius, comparing actual measurements (black dots) with predictions from the radial flow solution under the assumption of constant hydraulic properties (Sáez, 2023) (red line). Panel (b): Illustrates the pressure profile over the early-time injection period. The red line represents the model's prediction, while the black dots indicate actual pressure measurements. The divergence between the two highlights the model's limitation. Parameters of the fit: residual friction $f_r = 0.6$, residual distance to failure $f_r\sigma'_o - \tau_o = 0.5$ [MPa], and storage times thickness $S_e * w = 2 * 10^{-8}$ [m/Pa].

4. FIRST MODEL. AXISYMMETRIC FULLY COUPLED

We aim to simulate fracture propagation caused by fluid injection in the crystalline rock mass. In our formulation, the fault remains mechanically closed as the fluid pressure does not exceed the minimum confining stress, ensuring that we do not open the fracture (pure shear mode). We assume that the rock's permeability is low compared to that of the fracture, and we focus on the time scales during which fluid penetration into the formation is negligible, allowing us to disregard fluid leak-off.

We model the rock mass as a linearly elastic, homogeneous, and isotropic porous medium with a linear slip-weakening friction coefficient and variable permeability. The fault permeability can change due to 1) shear-induced dilation as well as 2) the nonlinear response of the normal effective stress contact (we use the Barton-Bandis model (Bandis, et al., 1983)). We consider the fracture to be a zero-thickness interface (we perform width averaging) and assume that all inelastic deformations are resolved on the fault plane. To capture the inelastic response of the fracture interface in contact, we employ a poroelasto-plastic interfacial constitutive law. We implement a non-associated Mohr-Coulomb failure criteria to model the fault element deformation from its shear activation. Finally, the fluid flow is restricted to the fracture filled zone, and its hydraulic transmissibility evolves with its aperture evolution (following the cubic law). Fluid flow in the granite matrix is neglected.

Using the exact injection schedule, we perform 3D axisymmetric hydromechanical simulations of the Basel hydraulic stimulation. As explained in Section 2, we begin our investigation with the model that accounts only for one group of events (the Red group).
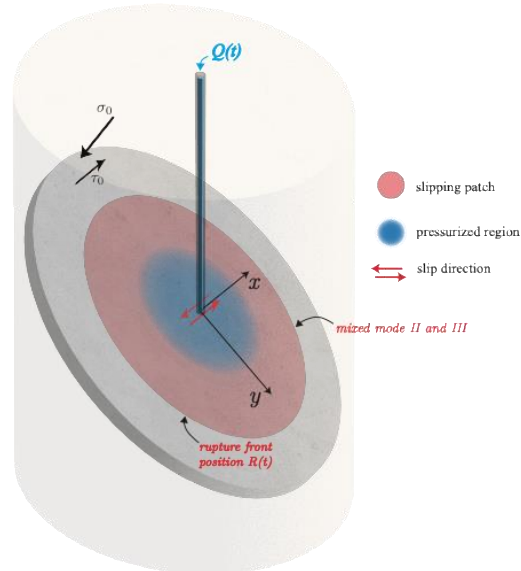

Figure 8: Model sketch. Fluid-induced frictional rupture (in red) propagating along a pre-existing fracture (in gray). Critically stressed regime: the rupture front is outpacing the fluid front.

9

4.1 Discussion on Model Parameters

The early-time dynamics of fluid-induced shear ruptures are significantly influenced by the peak stress-injection parameter, denoted as $\mathcal{T}_p$ (Sáez, et al., 2023), which is defined in terms of the peak friction coefficient f_p:

$$\mathcal{T}_p = \frac{(f_p \sigma_o' - \tau_o)}{f_p \Delta p_*} \tag{11}$$

where Δp_* represents the characteristic overpressure, quantifying the magnitude of the overpressure at the fluid source. The numerator of $\mathcal{T}_p$ represents the initial distance to failure, while the denominator characterizes the intensity of the injection.

A large value of $\mathcal{T}_p$ indicates a scenario where the injection rate is relatively low compared to the initial distance to failure $(f_p \sigma_o' - \tau_o)$, known as the marginally pressurized limit. In this regime, rupture propagation is primarily driven by the fluid and cannot surpass the pressure front. Conversely, a low $\mathcal{T}_p$ value (critically stressed limit) occurs when the injection rate is sufficiently high to create a significant overpressure at the fluid source, resulting in a $f_p \Delta p_*$ that exceeds the initial distance to failure. In this case, the rupture front moves faster than the fluid front, thereby aligning the pressure profile more closely to that of a point force.

In field applications, the system typically transitions from a marginally pressurized to a critically stressed limit with an increase in the injection rate. As the rupture progresses and the process zone becomes localized, the peak stress-injection parameter transitions to a residual stress-injection parameter $\mathcal{T}_r$:

$$\mathcal{T}_r = \frac{(f_r \sigma_o' - \tau_o)}{f_r \Delta p_*} \tag{12}$$

that influences system behavior in this case.

This parameter significantly influences the system's behavior during later stages of stimulation. To accurately capture the early-time behavior – prior to the localization of the process zone – it is necessary to have a precise estimate of the initial distance to failure. This task is particularly challenging as minor uncertainties in stress magnitudes can lead to substantially different estimates of $\mathcal{T}_p$. In Basel, the most accurate method for estimating the initial distance to failure, $(f_p \sigma_o' - \tau_o)$, can be derived from analyzing the overpressure record. Notably, a sudden decrease in pressure by 0.2 MPa, observed 20 minutes after the start of stimulation at a relatively moderate overpressure of 1.75 MPa, strongly suggests that shear-induced dilation contributed to this decrease. Indeed, had there been no alterations in permeability, the overpressure data would have aligned with analytical models based solely on fluid dynamics, using initial transmissibility value derived from the pre-stimulation test. However, we could not fit the overpressure record after 20 minutes of injection with any of the analytical solutions used previously (Van Everdingen, et al., 1949). The inability to reconcile the overpressure records post-pressure drop indicates a shift in the fault permeability.

We hypothesize that the fluid injected during the pre-stimulation test has migrated further along the fault, locally weakening the fault zone near the injection point while remaining sufficiently distant so as not to influence the overpressure measured at the surface. Considering this, we set the initial distance to failure along the fault at 2.75 MPa – a value slightly greater than that observed at the first pressure drop. Although we assign the same initial distance to failure to the entire fracture, it only plays a role at early times when the process zone has not yet localized. Thus, the value 2.75 MPa essentially represents an average distance to failure in the area where the hypothetical rupture is "small" – specifically, in the vicinity of the injection point. Subsequently, we fixed the peak friction coefficient at 0.66, a commonly used value that allows us to constrain the stress tensor given the known dip and azimuth of the red plane, and the established initial distance to failure.

Regarding the rupture radius, we utilize insights from the semi-analytical solution detailed in Equation (10), which indicates that the parameters governing the rupture front position for a given injected volume include the residual friction coefficient f_r, residual distance to failure $(f_r \sigma_o' - \tau_o)$, and the storage times thickness of the fluid flow zone $S_e * w$. Due to the lack of specific data on the actual thickness of the flow zone, we are unable to separate storage from thickness. Literature suggests storage coefficient values typically range from 10^{-12} to 10^{-10}. Given that the openhole section measures 371 meters in height and 22 cm in diameter, the fluid flow zone is likely concentrated around fractures and could span from centimeters to meters. To accurately model the evolution of the rupture radius, we adjust both the residual friction coefficient and the storage times thickness to fit observed data.

The best fitting parameters are presented in Table 3. We adjusted the parameters of the Barton-Bandis model, specifically the normal spring stiffness k_n and the maximum closure v_m, to reproduce the overpressure record at late times. To fit the early-time pressure response, we modified the dilation angle along with Young's modulus. Notably, Young's modulus is inversely proportional to the shear modulus, which influences the amount of slip; extensive slip accelerates dilatancy, leading to more abrupt pressure drops.

Table 3: Set of in-situ and material parameter used.

$S_V, [MPa]$	$S_{Hmax}, [MPa]$	$S_{hmin}, [MPa]$	$f_p, [-]$	$f_p \sigma_o' - \tau_o, [MPa]$
26.3z − 4	5z + 140	7z + 42	0.66	2.75

$E, [GPa]$	$\nu, [-]$	$\psi_p, [°]$	$d_c, [m]$	$f_r, [-]$
40	0	6°	0.0025	0.6
$k*h, [m^3]$	$C_d, [m^3 Pa^{-1}]$	$S_e*h, [m/Pa]$	$\mu, [Pa*s]$	$v_m, [m]$
$2*10^{-15}$	$6.5*10^{-8}$	$8*10^{-9}$	$2.5*10^{-4}$	0.00043
$k_n(\sigma'=0), [Pa/m]$	$k_s, [Pa/m]$	**Permeability model**	**Friction model**	**Dilatancy model**
$30*10^9$	$100*Young's$	cubic	linear	linear

4.2 Results for Axisymmetric Model

Figure 9 displays the numerical results for the injection overpressure and seismic radius related to the red group of events. It is essential to note that the recorded overpressure at the wellhead includes some anomalies that were not targeted in our model fit. Specifically, at around 160,000 seconds and 220,000 seconds, there are unexpected increases in pressure despite the injection rate remaining constant. Apart from these anomalies, the model generally captures well the over-pressure variation, with most deviations staying within 10% up to shut-in.

Post-shut-in discrepancies between the recorded data and the numerical simulation may arise from the nonlinear spring response under varying loading and unloading conditions, which requires additional investigation. At early times, the differences between the recorded pressure and the fit are linked to sudden increases in permeability due to dilation. While this observation suggests that further refinement of the dilation model might improve the fit, we opt not to pursue this to avoid overfitting the data.
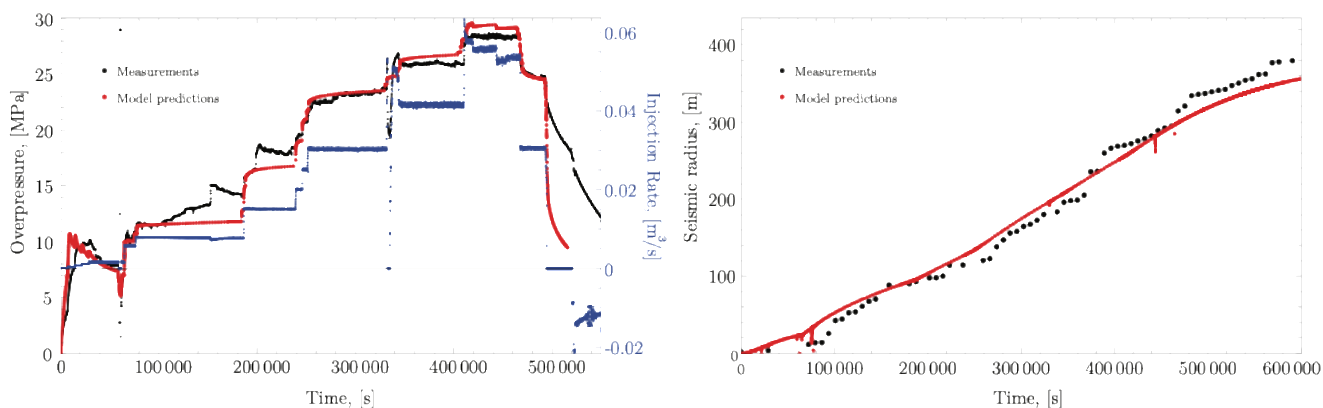

Figure 9. Panel (a): The graph illustrates the evolution of overpressure at the wellhead over time, plotted alongside the injection rate (blue line). Black dots represent measured overpressure values, and the red dots indicate model predictions. Panel (b): Panel: This graph shows the growth of the seismic radius over time, with black dots indicating measured values and the red dots representing model predictions.

5. CONCLUSIONS

The enhanced model, which accounts for dilation, permeability changes, and the nonlinearity of contact, successfully reproduces both the pressure record and the evolution of the seismic radius. This indicates that these factors are critical and sufficient for the purposes of hydraulic stimulation. There is no need to model the entire complexity of the seismic cloud to replicate the pressure record accurately.

REFERENCES

Giardini, D., Wiemer, S., Fäh, D. & Deichmann, . N., 2004. *Seismic Hazard Assessment of Switzerland. Swiss Seimological Service,* Switzerland: Swiss Seimological Service, ETH Zürich.

Ustazewski, K. & Schmid, S., 2007. Latest Pliocene to recent thick-skinned tectonics at the Upper Rhine Graben–Jura Mountains junction. *Swiss Journal of Geosciences,* p. 293–312.

Baisch, S. & Vörös, R., 2009. *Induced seismicity AP3000, Appendix 2,* s.l.: s.n.

Kaeser B., K. A. B. J., 2007. *The crystalline basement drilled at the Basel-1 geothermal site. A preliminary petrological geochemical study,* Neuchâtel, Switzerland: Institut de Géologie et d'Hydrogéologie, Université de Neuchâtel.

Fakhretdinova et al.

Ziegler, M., Valley, B. & Evans, K., 2015. *Characterisation of Natural Fractures and Fracture Zones of the Basel EGS Reservoir inferred from Geophysical Logging of the Basel-1 Well.* Melbourne, Australia, s.n., p. 12.

Ladner, F., Schanz, U. & Häring, M., 2008. Deep-Heat-Mining-Projekt Basel— Erste Erkenntnisse bei der Entwicklung eines Enhanced Geothermal System (EGS). *Bulletin Angew Geology,* p. 41–54.

Plenefisch, T. & Bonjer, K.-P., 1997. The stress field in the Rhine Graben area inferred from earthquake focal mechanisms and estimation of frictional parameters.. *Tectonophysics 275,* p. 71–97.

Kastrup, U., Zoback, M., Deichmann, N. & Evans, K., 2004. Stress field variations in the Swiss Alps and the northern Alpine foreland derived from inversion of fault plane solutions.. *Journal of Geophysical Research 109.*

Deichmann, N., Ballarin, D. & Kastrup, U., 2000. *Seismizität der Nord- und Zentralschweiz.,* Wettingen, Switzerland: s.n.

Dahrabou, . A. et al., 2022. A systematic methodology to calibrate wellbore failure models, estimate the in-situ stress tensor and evaluate wellbore cross-sectional geometry. International Journal of. *International Journal of Rock Mechanics and Mining Sciences.*

Valley, B. & Evans, K., 2009. Stress orientation to 5 km depth in the basement below Basel (Switzerland) from borehole failure analysis. *Swiss Journal of Geosciences,* p. 102.

Braun, R., 2007. *Analyse gebirgsmechanischer Versagenszustände beim Geothermieprojekt Basel ,* Basel, Switzerland: Consultancy in rock mechanics.

Häring, M., Schanz, U., Ladner, F. & Dyer, B., 2008. Characterisation of the Basel 1 enhanced geothermal system. *Geothermics,* pp. 469-495.

Dyer, B. et al., 2008. Microseismic Imaging of a Geothermal Reservoir Stimulation.. *The Leading Edge,* p. 856–869.

Dyer, B. et al., 2010. Application of microseismic multiplet analysis to the Basel geothermal reservoir stimulation events. *Geophysical Prospecting,* pp. 791-807.

Alcolea, A., Meier, P., Dyer, B. & Genoni, O., 2011. *Further evaluation of the Basel Microseismic Clusters. Characterization of the geometry of the stimulated reservoir and design criteria for seismic risk mitigation,* s.l.: s.n.

Dyer, B., 2008. *Investigation of the Waveforms of the Largest Seismic Events Due to the Basel 1 Stimulation, December 2006. Semore Seismic,* s.l.: Unpublished.

Viesca, R., 2021. Self-similar fault slip in response to fluid injection. *Journal of Fluid Mechanics.*

Sáez, A. & Lecampion, B., 2023. Post-injection aseismic slip as a mechanism for the delayed triggering of seismicity.

Deichmann, N. & Jacques, E., 2009. Earthquake Focal Mechanisms of the Induced Seismicity in 2006 and 2007 below Basel (Switzerland). *Swiss Journal of Geosciences.*

Van Everdingen, A. & Hurst, W., 1949. The Application of the Laplace Transformation to Flow Problems in Reservoirs. *Journal of Petroleum Technology,* p. 305–324.

Boyet, A., De Simone, S., Ge, S. & Vilarrasa, V., 2022. Insights on Post-Injection Seismicity through Analysis of the Enhanced Geothermal System at Basel (Switzerland).

Boyet , A., De Simone, S. & Vilar, V., 2023. Hydro-Mechanical Modeling of Injection-Induced Seismicity at the Deep Heat Mining Project of Basel, Switzerland.

Miller, S., 2012. Modeling Enhanced Geothermal Systems and the Essential Nature of Large-Scale Changes in Permeability at the Onset of Slip'.

Lei, Z., Ren, X., Zhou, J. & Li, H., 2022. Numerical Study on the Induced Seismicity through Hydraulic Fracturing in the Deep Heat Mining Project in Basel, Switzerland Using a Pseudo Dynamic Model and Considering Fully Hydro-Mechanical Coupling.

Terakawa, T., 2014. Evolution of Pore Fluid Pressures in a Stimulated Geothermal Reservoir Inferred from Earthquake Focal Mechanisms..

Terakawa, T., Miller, S. & Deichmann, N., 2012. High Fluid Pressure and Triggered Earthquakes in the Enhanced Geothermal System in Basel, Switzerland.

Mukuhira, Y. et al., 2017. Pore Pressure Behavior at the Shut-in Phase and Causality of Large Induced Seismicity at Basel, Switzerland.

Boyet, A., De Simone, S., Ge, S. & Vilarrasa, V., 2023. Poroelastic Stress Relaxation, Slip Stress Transfer and Friction Weakening Controlled Post-Injection Seismicity at the Basel Enhanced Geothermal System.

Sandro, A., Santillán, D. & Mosqu, J. C., 2019. Thermo-Poroelastic Analysis of Induced Seismicity at the Basel Enhanced Geothermal System.

Lei, Z. et al., 2016. Numerical Investigation of the Hydromechanical Response of a Natural Fracture during Fluid Injection Using an Efficient Sequential Coupling Model.

Lecampion, B. et al., To appear in 2025. Three dimensional Simulation of fluid-driven ruptures on pre-existing discontinuities.

Bourdet, D., Ayoub, J. & Plrard, Y., 1989. Use of pressure derivative in well-test interpretation..

Kachanov., C. S. a. M., 1991. A simple technique for finding effective elastic constants of cracked solids for arbitrary crack orientation statistics..

Garagash, D. & Germanovich, L., 2012. Nucleation and Arrest of Dynamic Fault Rupture on a Pressurized Fault. *J. of Geophysical research.*

Eissa, E. & Kazi, A., 1988. Relation between static and dynamic Young's moduli of rocks.

Sáez, A., 2023. Three-dimensional fluid-driven frictional ruptures: theory and applications.. *PhD thesis, EPFL.*

Sáez, A. & Lecampion, B., 2024. Fluid-driven slow slip and earthquake nucleation on a slip-weakening circular fault. *Journal of the Mechanics and Physics of Solids.*

Bandis, S., Lumsden, A. & Barton, N., 1983. Fundamentals of Rock Joint Deformation. *International Journal of Rock Mechanics and Mining Sciences.*